

Impedance Trajectory Analysis during Power Swing for Grid-Forming Inverter with Different Current Limiters

Yanshu Niu, *Student Member, IEEE*, Zhe Yang, *Member, IEEE*, and Bikash C. Pal, *Fellow, IEEE*

Abstract—Grid-forming (GFM) inverter-based resources (IBRs) are capable of emulating the external characteristics of synchronous generators (SGs) through the careful design of the control loops. However, the current limiter in the control loops of the GFM IBR poses challenges to the effectiveness of power swing detection functions designed for SG-based systems. Among various current limiting strategies, current saturation algorithms (CSAs), widely employed for their strict current limiting capability, are the focus of this paper. The paper presents a theoretical analysis of the conditions for entering and exiting the current saturation mode of the GFM IBR under three CSAs. Furthermore, the corresponding impedance trajectories observed by the distance relay on the GFM IBR side are investigated. The analysis results reveal that the unique impedance trajectories under these CSAs markedly differ from those associated with SGs. Moreover, it is demonstrated that the conventional power swing detection scheme may lose functionality due to the rapid movement of the trajectory or its failure to pass through the detection zones. Conclusions are validated through simulations in MATLAB/Simulink.

Index Terms—grid-forming control, current limiter, current saturation algorithm, power swing detection.

I. INTRODUCTION

TO achieve the net-zero commitment, inverter-based resources (IBRs) driven by renewable energy, such as wind and solar, are gradually replacing synchronous generators (SGs) powered by fossil fuels in power systems [1]. Although grid-following (GFL) remains the predominant control method for IBRs, grid-forming (GFM) more accurately mimics the rotor dynamic response of synchronous generators (SGs) [2, 3], on which conventional protection schemes are based. Therefore, compared to GFL IBRs, GFM IBRs are considered more effective in alleviating the potential risk of malfunctions in power swing detection functions as the penetration of IBRs increases [4]. However, differing from SGs, the external response of GFM IBRs is governed by control loops, lacking a rigid rotor body to provide inherent inertia. Moreover, to protect the power electronics components of the IBRs, the current limiter in the control loop restricts the current reference to the maximum allowable value. Consequently, how GFM IBRs influence power swing detection functions remains an unsolved mystery [4, 5], and further research is required to investigate the underlying mechanisms.

Power swing detection serves two primary functions: power swing blocking (PSB) and out-of-step tripping (OST). The PSB function aims to discriminate between a fault and a power swing, blocking the distance protection to prevent unnecessary

tripping if the event is determined to be a power swing rather than a fault [6]. The objective of the OST function is to distinguish between stable and unstable power swings, separating the system at pre-selected network locations to prevent further cascading faults in the event of an unstable power swing [7, 8]. Mature power swing detection methods include traditional approaches, such as those based on the rate of change of impedance or resistance, as well as non-traditional approaches designed for microprocessor-based relays [7–10]. These non-traditional approaches include continuous impedance calculation, continuous incremental current calculation, and synchrophasor-based out-of-step relaying, among others [10]. The methods based on the rate of change of apparent impedance are still the mainstream methods in commercial relays, and the blinder-based methods are the most widely applied [11–13]. According to the guideline published by the IEEE Standards Association, the three-step operation mode in the blinder-based methods is recommended, as it provides more accurate detection of persistent and slow-moving apparent impedance trajectories [14]. Additionally, this method enables the simultaneous implementation of both PSB and OST functions [11]. However, this method may lose functionality because of the current limiting of GFM IBRs.

To prevent overcurrent from causing damage to the power electronic components in GFM IBRs, current saturation algorithms (CSAs) and virtual impedance (VI) methods are widely applied to limit the current [15–17]. This paper focuses on three typical CSAs: circular CSA, d-axis priority CSA, and q-axis priority CSA. Limited research has investigated the conditions for exiting the current saturation mode. The authors in [16] assume that the current exits the saturation mode at the intersection point of the P- δ curves under saturated and unsaturated modes. Although the simulation-based case studies in [16] seem to verify this assumption, a theoretical analysis is lacking to prove it. The fault recovery process under the constant CSA has been analysed in [18], revealing the differing conditions for the transition from normal operating mode to current saturation mode, and from current saturation mode back to normal operating mode. However, further theoretical analysis and a closed-form expression are not provided. It is highlighted in [19–21] that IBRs can potentially fall into saturated stable equilibrium points (SSEPs) during fault recovery, and the conditions for exiting the current saturation mode are also derived. However, the analysis only addresses the user-defined current angle in constant CSA, without considering the other three types of CSAs. The exiting conditions under

other different CSAs, which remain not well understood, significantly impact the apparent impedance trajectories during power swing.

Some research has preliminarily explored the impact of replacing SGs with renewable energy resources or IBRs on power swing detection. The influence of Type-III wind turbine generators on power swing detection was investigated in [22], and the scope was further extended to more general IBRs in [23]. However, these analyses are based solely on simulations, without providing theoretical explanations to reveal the underlying mechanism. A method is proposed to discriminate between symmetrical faults and power swings in [24], but the research scope remains limited to Type-III wind turbine generators. Simulations presented in [25] demonstrate that the rate of change of apparent impedance during stable and unstable power swings is significantly faster in GFL IBR-based systems than in systems with only SGs. This rapid rate of change poses a risk of PSB and OST malfunctions. From a more theoretical perspective, a dynamic model is developed in [26] to illustrate that the DC-link voltage control dynamics can significantly amplify the rate of impedance change [27]. The authors of [28] and [29] conducted a detailed theoretical analysis of power swing trajectories caused by IBRs and qualitatively investigated the influence of control parameters. However, the analyses in [25–29] are limited to GFL IBRs and do not address GFM IBRs. Although GFM IBRs are included in the research scope in [30], it does not account for the role of the current limiter. To the best of the authors' knowledge, no previous study has theoretically analysed the power swing trajectories of GFM IBRs under CSA-based current-limiting strategies.

To fill this gap, the apparent impedance trajectories of the GFM IBR during power swings under three types of CSA are analysed in this paper. Furthermore, the impact of these trajectories on legacy power swing detection protection is investigated. The main contributions of this paper are as follows:

- The conditions for entering and exiting current saturation mode are derived for three types of CSAs: circular, d-axis priority, and q-axis priority. The analysis reveals that the entering and exiting angle sets are not complementary to each other.
- The full-cycle power swing trajectories under these three CSA strategies are examined. The analysis highlights their distinct characteristics compared to those of conventional SG-based systems.
- The impact of different CSAs on system stability is investigated. Additionally, the influence of the impedance trajectories associated with CSAs is explored. The results indicate that CSAs may deteriorate system stability and pose risks of malfunction in power swing detection.

The theoretical analysis is validated through a simulation model implemented on the MATLAB/Simulink platform.

The paper is organised as follows. In Section II, the system model with control loops is elaborated. In Section III, three typical CSAs are introduced, and the conditions for entering and exiting current saturation mode are derived. Section IV discusses the power swing trajectories with and without the

CSAs. Section V presents the simulation and case studies to validate the theoretical analysis. Finally, Section VI concludes the paper.

II. SYSTEM MODEL

Fig. 1(a) shows the system configuration of a grid-connected GFM IBR system. The DC source is connected to the grid through an inverter, an LC filter, a step-up transformer Z_{tr} and a transmission line Z_l . The grid is modeled as a Thevenin equivalent voltage source $V_g \angle \theta_g$ in series with an impedance Z_g . The low-voltage side of the transformer is considered as the point of common coupling (PCC). Thus, the total impedance between the PCC and the Thevenin equivalent voltage source of the grid is $Z_{tr} + Z_l + Z_g = Z_T \angle \phi = R_T + jX_T$. The phase angle of the GFM IBR, θ , is generated by the active power controller (APC) in the virtual synchronous machine control scheme to emulate the swing equations of the SGs; while the voltage set point of the GFM IBR should be determined by the reactive power controller (RPC). However, as RPC is not the focus of this paper, the voltage set point is assumed to be $\dot{V}^{\text{ref}} = V_d^{\text{ref}} + jV_q^{\text{ref}} = 1 + j0$. With the local voltage reference of the GFM IBR aligned along the d-axis, where $\theta = 0$, the power angle between the IBR and the grid is defined by $\delta = \theta - \theta_g$, i.e., $\delta = -\theta_g$. A distance protection relay is installed at the transmission line terminal near the transformer, equipped with both distance protection and power swing detection functions.

A typical voltage-current dual-loop cascaded control structure is implemented in this paper, as illustrated in Fig. 1(b). To prevent overcurrent in any abnormal operating condition from damaging the power electronic components in the inverter, a CSA is essential. It limits the magnitude of the current reference output from the voltage controller to the maximum allowable value I_{max} , generating a new current reference as the input to the current controller. To prevent integrator windup, the clamping anti-wind up technique is employed within the voltage PI controller to limit the magnitude of the PI output to u_{max} . The CSA can be implemented by prioritising the current vector angle, d-axis current and q-axis current, as presented in Fig. 2. These different algorithms have distinct conditions for exiting current saturation, which are reflected in different apparent impedance trajectories and will be investigated in the next sections.

III. CURRENT SATURATION ALGORITHM

In this section, the condition for entering current saturation is derived, followed by the analysis of the conditions for exiting saturation under different CSAs.

A. Condition for Entering Current Saturation

Independent of the specific CSA employed, the condition for entering current saturation remains consistent and can be expressed as:

$$i_{sd}^2 + i_{sq}^2 > I_{\text{max}}^2. \quad (1)$$

Based on (1) and Kirchhoff voltage law, the GFM IBR enters current saturation if

$$\cos \delta < \frac{|v_d^{\text{ref}}|^2 + |\dot{V}_g|^2 - (|Z_T|I_{\text{max}})^2}{2|v_d^{\text{ref}}||\dot{V}_g|}. \quad (2)$$

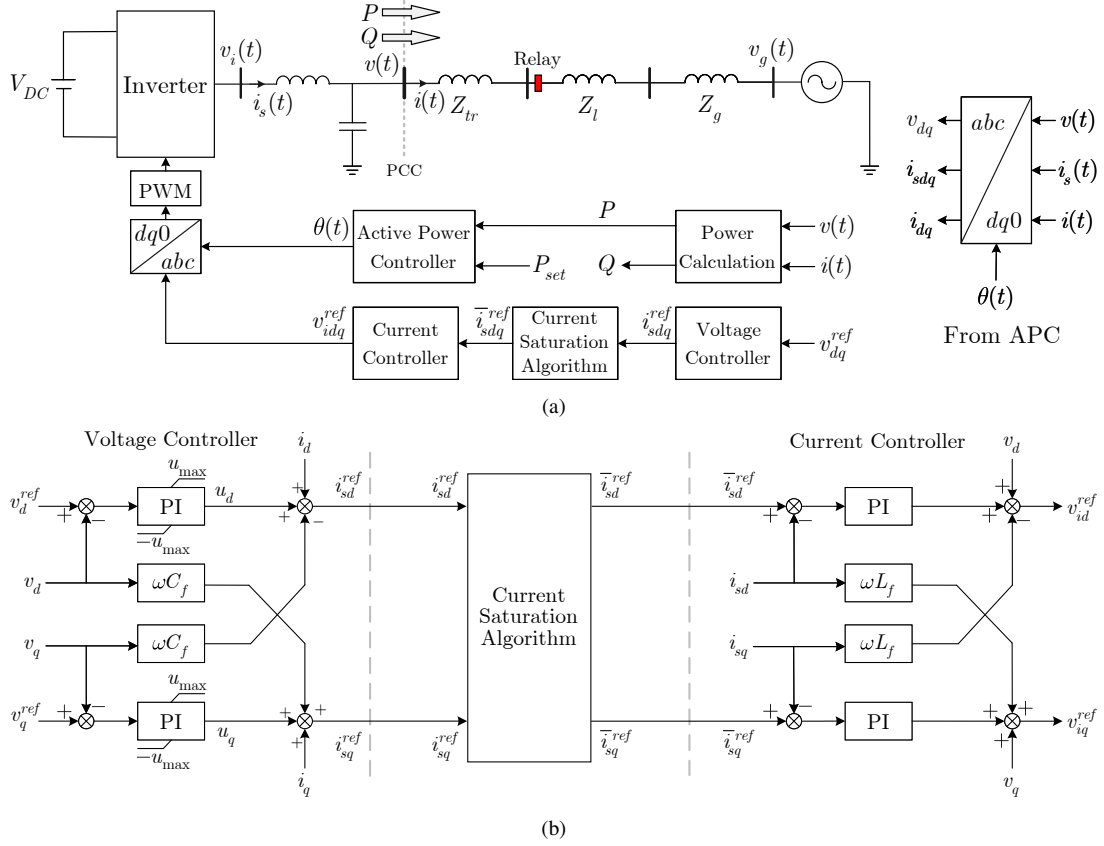


Fig. 1: Grid-connected GFM IBR system. (a) System model and control structure. (b) Control block diagram.

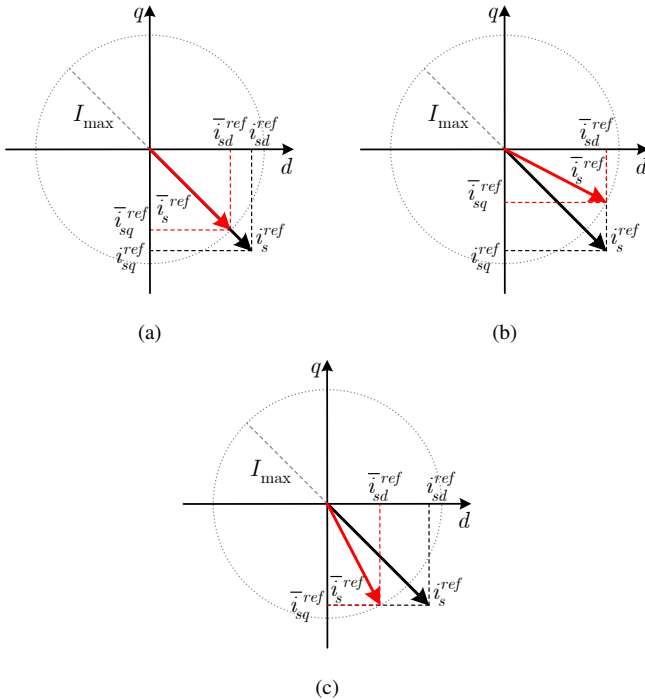


Fig. 2: The new current references generated by the CSAs. (a) Circular. (b) D-Axis Priority. (c) Q-Axis Priority.

The power angle at the critical condition where the current transitions from unsaturated to saturated is defined as

$$\delta_{\text{enter}} := \arccos \left[\frac{|v_d^{\text{ref}}|^2 + |\dot{V}_g|^2 - (|Z_T| I_{\text{max}})^2}{2|v_d^{\text{ref}}| |\dot{V}_g|} \right]. \quad (3)$$

Thus, when

$$\delta \in [\delta_{\text{enter}}, 2\pi - \delta_{\text{enter}}], \quad (4)$$

the power angle satisfies the condition for current saturation.

B. Conditions for Exiting Current Saturation

The conditions for exiting current saturation are not inherently complementary to those for entering saturation. Instead, they depend on the CSAs, as will be elaborated in the following discussion.

1) *Circular Current Saturation Algorithm*: Fig. 2(a) illustrates the priority of the current angle, referred to as the circular CSA, which limits the magnitude to I_{max} while maintaining the angle consistent with the unsaturated current reference before the current limiter. Under this algorithm, the generated d-axis and q-axis current references are

$$\bar{i}_{sd}^{\text{ref}} = \frac{i_{sd}^{\text{ref}}}{|i_{sd}^{\text{ref}}|} \times \min \left(|i_{sd}^{\text{ref}}|, |i_{sd}^{\text{ref}}| \times \frac{I_{\text{max}}}{\sqrt{(i_{sd}^{\text{ref}})^2 + (i_{sq}^{\text{ref}})^2}} \right) \quad (5)$$

$$\bar{i}_{sq}^{\text{ref}} = \frac{i_{sq}^{\text{ref}}}{|i_{sq}^{\text{ref}}|} \times \min \left(|i_{sq}^{\text{ref}}|, |i_{sq}^{\text{ref}}| \times \frac{I_{\text{max}}}{\sqrt{(i_{sd}^{\text{ref}})^2 + (i_{sq}^{\text{ref}})^2}} \right). \quad (6)$$

When the current enters the saturation mode, v_d and v_q cannot track their references, causing the rapid clamping of the PI controllers in the voltage control loops. Thus, the current references for the d-axis and q-axis before the CSA are

$$\bar{i}_{sd}^{\text{ref}} = \text{sgn}(u_d) u_{\max} + \bar{i}_{sd} \quad (7)$$

$$\bar{i}_{sq}^{\text{ref}} = \text{sgn}(u_q) u_{\max} + \bar{i}_{sq}, \quad (8)$$

where $\bar{i}_{sd} = \bar{i}_d - v_q \omega C_f$ and $\bar{i}_{sq} = \bar{i}_q + v_d \omega C_f$. Assuming that the response of the current controller is fast enough to accurately track the references, i.e., $\bar{i}_{sdq} = \bar{i}_{sdq}^{\text{ref}}$, it can be derived that

$$\left(\frac{1}{k} - 1\right) \bar{i}_{sd}^{\text{ref}} = \text{sgn}(u_d) u_{\max} \quad (9)$$

$$\left(\frac{1}{k} - 1\right) \bar{i}_{sq}^{\text{ref}} = \text{sgn}(u_q) u_{\max}, \quad (10)$$

where $k = I_{\max} / \sqrt{(i_{sd}^{\text{ref}})^2 + (i_{sq}^{\text{ref}})^2}$. The sign of u_d depends on the sign of $(v_d^{\text{ref}} - v_d)$ according to the voltage control loop in Fig. 1(b); similarly, the sign of u_q depends on the sign of $(v_q^{\text{ref}} - v_q)$, where v_d and v_q refer to the d-axis and q-axis components of the PCC voltage, denote as

$$v_d = v_g \cos \delta + |Z_T| (\bar{i}_{sd} \cos \phi - \bar{i}_{sq} \sin \phi), \quad (11)$$

$$v_q = -v_g \sin \delta + |Z_T| (\bar{i}_{sd} \sin \phi + \bar{i}_{sq} \cos \phi). \quad (12)$$

Since $k \leq 1$ under the saturation mode, the magnitude of the d-axis and q-axis currents satisfy

$$|\bar{i}_{sd}| = |\bar{i}_{sq}| = \frac{\sqrt{2}}{2} I_{\max}. \quad (13)$$

The signs of \bar{i}_{sd} and \bar{i}_{sq} are consistent with those of u_d and u_q , respectively. Therefore, when the current has not exited saturation, that is, when v_d and v_q fail to simultaneously track their respective references, the signs of \bar{i}_{sd} or \bar{i}_{sq} may change with the variation of the phase angle θ_g of V_g , as illustrated in the example shown in Fig. 3. As the power angle δ increases

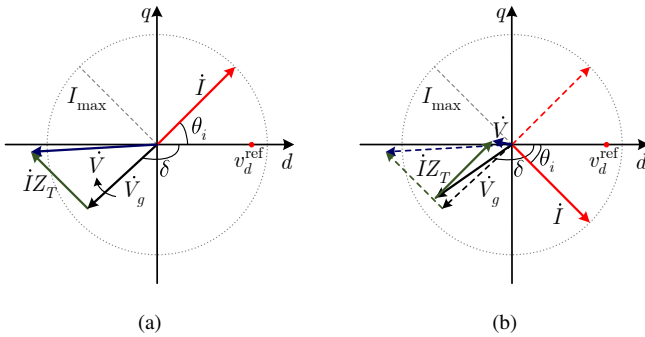


Fig. 3: The process of a change in the sign of \bar{i}_{sq} . (a) Before v_q tracks v_q^{ref} . (b) After v_q tracks v_q^{ref} , as indicated by the solid lines.

in the Fig. 3(a), the grid voltage \dot{V}_g rotates counterclockwise. Before v_q can track the reference v_q^{ref} , $v_q^{\text{ref}} - v_q$ is positive, resulting in a positive \bar{i}_{sq} . Similarly, \bar{i}_{sd} remains positive. Thus, the saturated current is located in the first quadrant. As \dot{V}_g continues to rotate, moving the phasor \dot{V} into the second quadrant as shown in Fig. 3(b), $v_q^{\text{ref}} - v_q$ changes from positive to negative, causing \bar{i}_{sq} to also become negative, while \bar{i}_{sd}

remains positive. Consequently, the saturated current jumps from the first quadrant to the fourth quadrant. The sudden change in the current leads to a significant reduction in the magnitude of \dot{V} , as illustrated in the figure.

Because the saturated current exhibits a sudden change before and after the d-axis or q-axis voltage tracks its reference, only two possible scenarios exist under circular CSA control where both d-axis and q-axis voltages simultaneously track their relative references, as shown in Fig. 4. Just before v_q

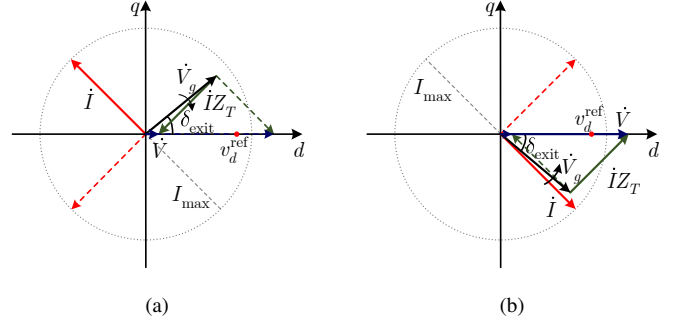


Fig. 4: Two scenarios for current exiting saturation under circular CSA control. The dashed lines represent the moment just before v_q tracks v_q^{ref} , while the solid lines represent the moment just after v_q tracks v_q^{ref} . (a) \dot{V}_g rotates clockwise. (b) \dot{V}_g rotates counterclockwise.

tracks v_q^{ref} , the saturated current \dot{I} and the PCC voltage \dot{V} are located at the positions indicated by the red dashed line and the blue dashed line in Fig. 4, respectively. Once v_q successfully tracks v_q^{ref} , the sign of \bar{i}_{sq} changes, resulting \dot{I} and \dot{V} rapidly shift to the positions marked by the red solid line and the blue solid line. During this transition, \dot{V} passes through the PCC voltage set point v_{dq}^{ref} , thereby satisfying the exit condition and enabling the current to exit saturation. The clockwise and counterclockwise variations of δ shown in the figure share the same exit condition, which is

$$-V_g \sin \delta + \frac{\sqrt{2}}{2} I_{\max} |Z_T| \cos \phi + \frac{\sqrt{2}}{2} I_{\max} |Z_T| \sin \phi = v_q^{\text{ref}} = 0. \quad (14)$$

Defining

$$\delta_{\text{exit}}^{\text{circular}} := \arcsin \left[\frac{\sqrt{2} I_{\max} |Z_T| (\cos \phi + \sin \phi)}{2 V_g} \right], \quad (15)$$

the set of power angles δ that enable the current to exit the saturation mode under circular SCA control is given by

$$\delta \in [0, \delta_{\text{exit}}^{\text{circular}}] \cup [2\pi - \delta_{\text{exit}}^{\text{circular}}, 2\pi]. \quad (16)$$

2) *D-Axis Priority Current Saturation Algorithm*: With the d-axis priority current saturation algorithm shown in Fig. 2(b), the d-axis and q-axis current references are as follows.

$$\bar{i}_{sd}^{\text{ref}} = \frac{i_{sd}^{\text{ref}}}{|i_{sd}^{\text{ref}}|} \times \min(|i_{sd}^{\text{ref}}|, I_{\max}) \quad (17)$$

$$\bar{i}_{sq}^{\text{ref}} = \frac{i_{sq}^{\text{ref}}}{|i_{sq}^{\text{ref}}|} \times \min\left(|i_{sq}^{\text{ref}}|, \sqrt{(I_{\max})^2 - (\bar{i}_{sd}^{\text{ref}})^2}\right). \quad (18)$$

After the current is limited, the GFM IBR can exit the saturation mode, if

$$(i_{sd}^{\text{ref}})^2 + (i_{sq}^{\text{ref}})^2 < I_{\max}^2, \quad (19)$$

where i_{sd}^{ref} and i_{sq}^{ref} are expressed as (7) and (8). With the saturation of the current, the voltages on the d-axis and q-axis can not track their respective voltage references. Consequently, the integrators within the PI controllers of the voltage loops, as shown in Fig. 1(b), will clamp promptly, reaching their maximum output, u_{max} . Thus, the condition for exiting the saturation has the same expression as

$$[\text{sgn}(u_d) u_{\text{max}} + \text{sgn}(\bar{i}_{sd}) I_{\text{max}}]^2 + [\text{sgn}(u_q) u_{\text{max}}]^2 < I_{\text{max}}^2. \quad (20)$$

Assuming that $u_{\text{max}} \ll I_{\text{max}}$, it is derived that

$$\text{sgn}(u_d) \text{sgn}(\bar{i}_{sd}) < 0. \quad (21)$$

There are two cases that can address the above inequality.

$$\text{Case 1: } u_d < 0, \bar{i}_{sd} = +I_{\text{max}}; \quad (22)$$

$$\text{Case 2: } u_d > 0, \bar{i}_{sd} = -I_{\text{max}}. \quad (23)$$

In Case 2, the solution does not exist; therefore, the solution in Case 1 yields a unique exit condition, which is

$$\cos \delta > \frac{|v_d^{\text{ref}}| - |Z_T| I_{\text{max}} \cos \phi}{|\bar{V}_g|}. \quad (24)$$

Defining

$$\delta_{\text{exit}}^{\text{d-axis}} := \arccos \left[\frac{|v_d^{\text{ref}}| - |Z_T| I_{\text{max}} \cos \phi}{|\bar{V}_g|} \right], \quad (25)$$

the power angle set of exiting the current saturation with d-axis priority CSA is

$$\delta \in [0, \delta_{\text{exit}}^{\text{d-axis}}] \cup [2\pi - \delta_{\text{exit}}^{\text{d-axis}}, 2\pi] \quad (26)$$

3) *Q-Axis Priority Current Saturation Algorithm*: If the q-axis current reference is prioritised for current limiting, as shown in Fig. 2(c), the d-axis and q-axis references generated by current limiter are

$$\bar{i}_{sd}^{\text{ref}} = \frac{i_{sd}^{\text{ref}}}{|i_{sd}^{\text{ref}}|} \times \min \left(|i_{sd}^{\text{ref}}|, \sqrt{(I_{\text{max}})^2 - (\bar{i}_{sq}^{\text{ref}})^2} \right) \quad (27)$$

$$\bar{i}_{sq}^{\text{ref}} = \frac{i_{sq}^{\text{ref}}}{|i_{sq}^{\text{ref}}|} \times \min \left(|i_{sq}^{\text{ref}}|, I_{\text{max}} \right) \quad (28)$$

The condition for current exiting saturation under q-axis priority CSA control is similar to that under d-axis priority. At the moment of exiting saturation, the signs of u_q and \bar{i}_{sq} satisfy the relationship

$$\text{sgn}(u_q) \text{sgn}(\bar{i}_{sq}) < 0. \quad (29)$$

It can be discussed in two cases:

$$\text{Case 1: } u_q < 0, \bar{i}_{sq} = +I_{\text{max}}; \quad (30)$$

$$\text{Case 2: } u_q > 0, \bar{i}_{sq} = -I_{\text{max}}. \quad (31)$$

The solutions corresponding to the two cases are

$$\sin \delta > -\frac{|Z_T| I_{\text{max}} \cos \phi}{|\bar{V}_g|} \quad (32)$$

and

$$\sin \delta < \frac{|Z_T| I_{\text{max}} \cos \phi}{|\bar{V}_g|}, \quad (33)$$

respectively. Defining

$$\delta_{\text{exit}}^{\text{q-axis}} := \arcsin \left[\frac{|Z_T| I_{\text{max}} \cos \phi}{|\bar{V}_g|} \right], \quad (34)$$

the current can exit the saturation mode, if the power angle belongs to the set

$$\delta \in [0, \delta_{\text{exit}}^{\text{q-axis}}] \cup [\pi - \delta_{\text{exit}}^{\text{q-axis}}, \pi + \delta_{\text{exit}}^{\text{q-axis}}] \cup [2\pi - \delta_{\text{exit}}^{\text{q-axis}}, 2\pi] \quad (35)$$

However, it is worth noting that the exit angle set $\delta \in [\pi - \delta_{\text{exit}}^{\text{q-axis}}, \pi + \delta_{\text{exit}}^{\text{q-axis}}]$ also belongs to the saturation angle set. When the power angle is within this set, both the entering and the exiting saturation conditions are simultaneously satisfied, causing the IBR to oscillate between the two modes, which negatively impacts system stability. To eliminate the oscillation, within this subset, forced saturation is implemented as follows.

$$\bar{i}_{sq} = +I_{\text{max}}, \quad \text{if } \delta \in [\pi - \delta_{\text{exit}}^{\text{q-axis}}, \pi]; \quad (36)$$

$$\bar{i}_{sq} = -I_{\text{max}}, \quad \text{if } \delta \in [\pi, \pi + \delta_{\text{exit}}^{\text{q-axis}}]. \quad (37)$$

Therefore, the set of power angles for exiting saturation under q-axis priority CSA control is

$$\delta \in [0, \delta_{\text{exit}}^{\text{q-axis}}] \cup [2\pi - \delta_{\text{exit}}^{\text{q-axis}}, 2\pi]. \quad (38)$$

IV. ANALYSIS OF POWER SWING TRAJECTORIES

The power swing trajectories can be affected by different CSAs. In this section, the trajectory in the absence of current saturation is introduced, followed by a discussion of the trajectories under the three types of CSAs. The analysis in this section is based on the model in Fig. 5, which is the equivalent model shown in Fig. 1(a).

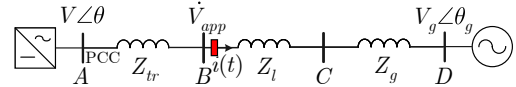


Fig. 5: A Single Machine GFM IBR Grid-Connected System.

A. Current Unsaturation

Under the assumptions that there is no current limitation in the control loops and that $|\bar{V}| = |\bar{V}_g|$, the apparent impedance observed by the relay near Bus B, marked in red in Fig. 5, is consistent with that in a SG-based system, as derived in [31]:

$$Z_{\text{app}} = \left(Z_l + Z_g - \frac{1}{2} Z_T \right) - j \frac{1}{2} Z_T \cot \frac{\delta}{2}. \quad (39)$$

Accordingly, with point B as the origin, the trajectory of the apparent impedance on the impedance plane is shown in Fig. 6. The green vector \overrightarrow{BP} represents the apparent impedance measured by the relay, and $\angle APD$ reflects the power angle δ between the GFM IBR and the grid. As δ increases from 0 to 2π , the apparent impedance endpoint P moves along OO' from right to left. The trajectory OO' is the perpendicular bisector of the line segment AD , which represents the total impedance between the PCC and the equivalent voltage source of the grid. Therefore, $|DP| = |AP|$. The figure illustrates that the apparent impedance \overrightarrow{BP} is uniquely mapped to the power angle δ , and this relationship can be effectively represented on the impedance plane. The conventional power swing detection scheme is based on this well-established property.

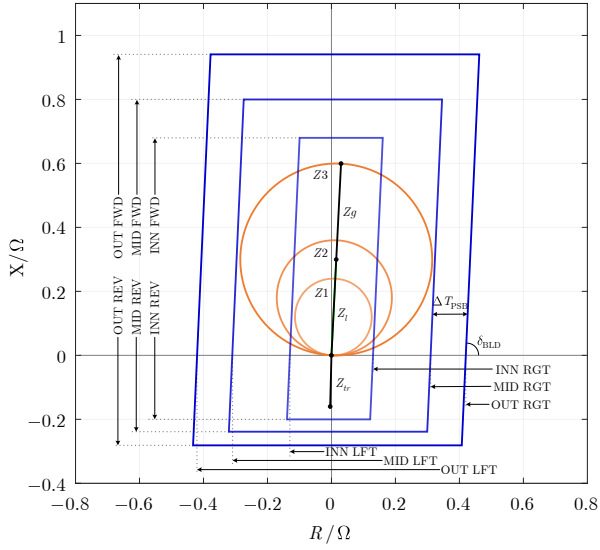


Fig. 8: The three-zone mho characteristics in distance protection and the three-step blinder characteristics in power swing detection.

TABLE I: Parameters of the test system and protection system settings

Parameters	Description	Value
System Configuration		
P_0	Active power set point	0.6 p.u.
f_n	Nominal frequency	60 Hz
V_d^{ref}	PCC voltage set point	1 p.u.
Z_g	Impedance of the generator	$0.3 \angle 84.26$ p.u.
Z_l	Impedance of the line	$0.3 \angle 84.26$ p.u.
Z_{tr}	Impedance of the transformer	$0.16 \angle 88.57$ p.u.
$\angle \phi$	Impedance angle of Z_T	87.44°
I_{max}	Overcurrent limitation	1.2 p.u.
u_{max}	Maximum magnitude of the output from the voltage PI controllers	0.063 p.u.
Distance Protection Setting		
Z1	80% of Z_l	$0.24 \angle 84.26$ p.u.
TD1	Zone1 time delay	0 s
Z2	120% of Z_l	$0.36 \angle 84.26$ p.u.
TD2	Zone2 time delay	0.5 s
Z3	200% of Z_l	$0.6 \angle 84.26$ p.u.
TD3	Zone3 time delay	1 s
Power Swing Detection Setting		
OUT RGT	Outer right blinder	0.42 p.u.
OUT LFT	Outer left blinder	-0.42 p.u.
MID RGT	Middle right blinder	0.31 p.u.
MID LFT	Middle left blinder	-0.31 p.u.
INN RGT	Inner right blinder	0.13 p.u.
INN LFT	Inner left blinder	-0.13 p.u.
OUT FWD	Outer forward reach	0.94 p.u.
OUT REV	Outer reverse reach	-0.28 p.u.
MID FWD	Middle forward reach	0.80 p.u.
MID REV	Middle reverse reach	-0.24 p.u.
INN FWD	Inner forward reach	0.68 p.u.
INN REV	Inner reverse reach	-0.20 p.u.
δ_{BLD}	The angles of right and left blinders	87.44°
ΔT_{PSB}	Power swing detection time threshold	0.033 s

of a current limiter, while the red lines correspond to the respective CSAs. The solid part of the lines indicates that the system can remain in this mode; the dashed part indicates that the system will exit this mode. It is obvious that the red lines, which represent the active power under the saturation modes, shrink the stable margin and therefore deteriorate the power system stability.

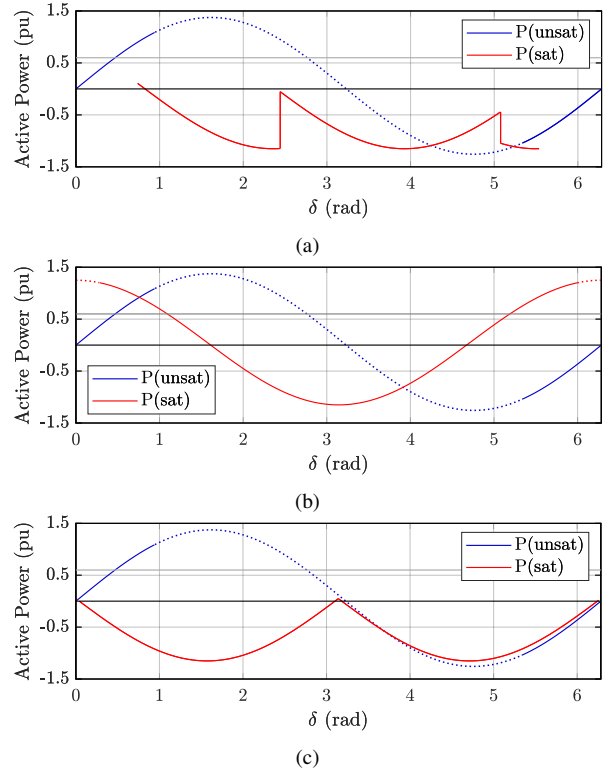


Fig. 9: $P - \delta$ curves for the three types of CSAs. (a) Circular. (b) D-Axis Priority. (c) Q-Axis Priority.

To verify the impact of CSAs on system stability, Cases 1 through 4 are established under the following conditions.

- Case 1: Operating as a virtual synchronous machine without considering CSA, $\Delta P_0 = +0.5$ pu at $t = 4$ s.
- Case 2: Circular CSA, $\Delta P_0 = +0.5$ pu at $t = 4$ s.
- Case 3: D-axis priority CSA, $\Delta P_0 = +0.5$ pu at $t = 4$ s.
- Case 4: Q-axis priority CSA, $\Delta P_0 = +0.5$ pu at $t = 4$ s.

The system configuration and other settings are identical to those listed in TABLE I. The apparent impedance trajectories on the impedance plane for the four cases are shown in Fig. 10. Under the same active power reference change conditions in the four cases, only Case 1, without considering the current limiter, allows the system to reach the new stable equilibrium point (SEP). Cases 2 to 4, which are equipped with different types of CSAs, cause the system to lose synchronisation. Cases 2 to 4 also demonstrate that under different CSAs, the saturation exiting angles are distinct. These differences are reflected on the impedance plane as variations in the specific points where the trajectories exit the circular path. The locations of these exit points are determined by both δ_{exit} and θ_i . Fig. 11 shows the curves of active power variation over time in Cases 1 to 4. It further verifies that only in Case 1, where the current limiter is not considered, the system can reach the new SEP, while the active power variations in Cases 2 to 4 align with the theoretical curves presented in Fig. 9. The theoretical saturation entry and exit angles, along with their corresponding simulation results as shown in the trajectories of Fig. 10, are presented in TABLE II. The theoretical values are verified against the simulation results.

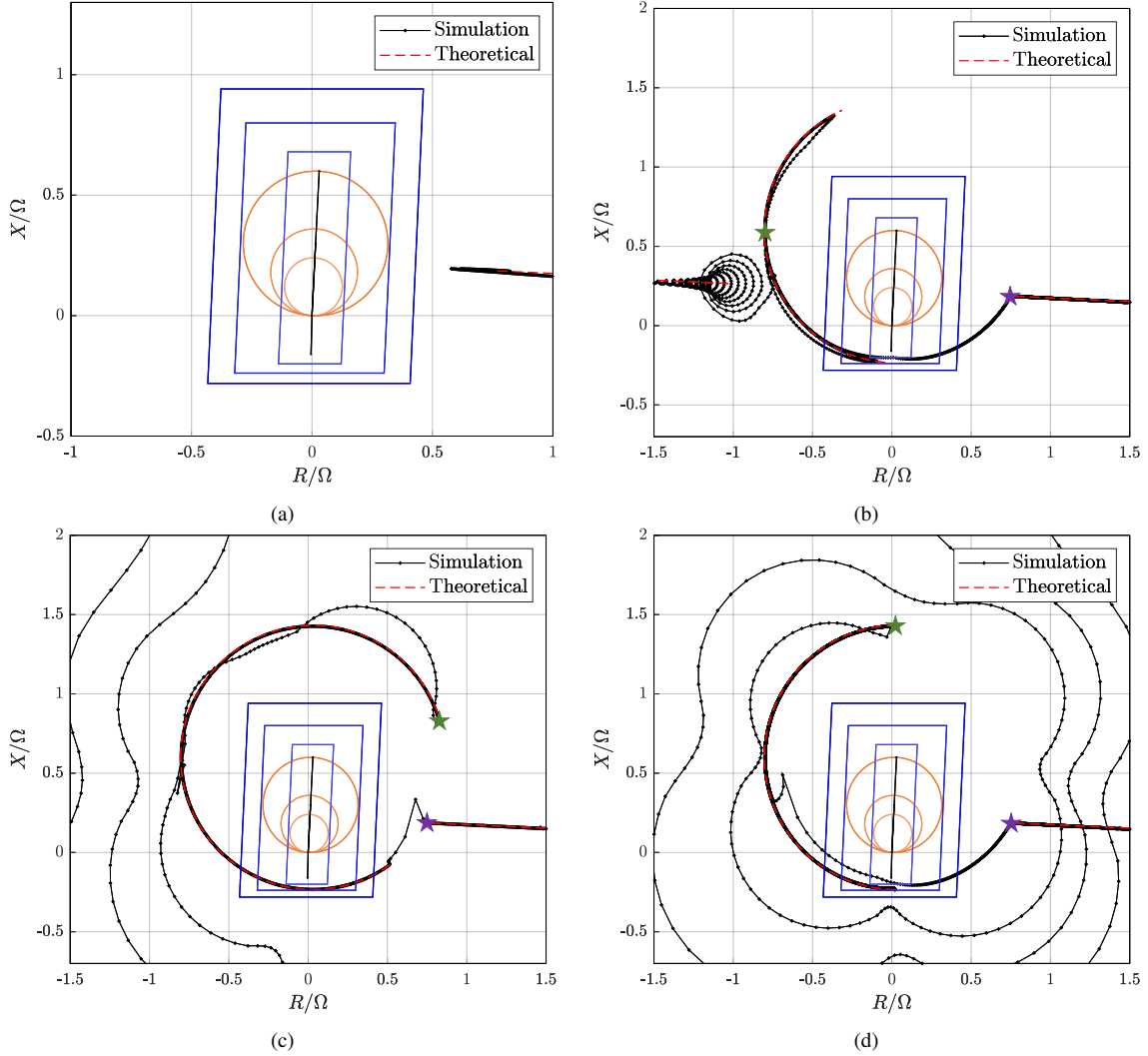


Fig. 10: The apparent impedance trajectories for Cases 1 to 4. The purple stars indicate the critical points where the current enters saturation, while the green stars mark where it exits saturation. (a) Case 1: Without CSA. (b) Case 2: Circular CSA. (c) Case 3: D-Axis Priority CSA. (d) Case 4: Q-Axis Priority CSA.

TABLE II: Critical angles for entering and exiting saturation under different CSAs in Cases 1 to 4, based on the parameters in TABLE I.

Unit: deg ($^{\circ}$)	Circular	D-Axis Priority	Q-Axis Priority
Theoretical Values			
δ_{enter}	54.26	54.26	54.26
δ_{exit}	± 42.30	± 16.41	± 2.34
$\delta_{\text{exit}} + \theta_i$	182.70	343.59	267.77
Simulation Results			
δ_{enter}	54.44	54.66	54.94
δ_{exit}	316.40	342.90	357.50
$\delta_{\text{exit}} + \theta_i$	179.10	343.80	269.80

C. The Impact of CSAs on Power Swing Detection

The new features of apparent impedance trajectories introduced by CSAs can cause power swing detection to malfunction under certain conditions. Cases 5 and 6 illustrate two typical scenarios.

- Case 5: D-axis priority CSA. $Z_g = 0.2 pu$; $Z_l = 0.2 pu$. Phase jump of -69.9° at $t = 4s$. The power swing detection blinders settings are adjusted in this case study,

maintaining the same proportional relationship with the 3-zone distance protection mho characteristics as presented in TABLE I.

- Case 6: D-axis priority CSA. $P_0 = 0.1 pu$; $I_{\text{max}} = 1.5 pu$. Phase jump of -69.9° at $t = 4s$.

The other conditions and settings remain consistent with those in TABLE I. Fig. 12 shows the apparent impedance trajectory of Case 5. It can be observed that the full-cycle trajectory remains outside the three-step blinders, meaning that neither stable nor unstable power swings can be correctly detected, resulting in the failure of both PSB and OST. Fig. 13 shows the apparent impedance trajectory in Case 6. Under the conditions of Case 6, the event is a stable power swing. However, due to the rapid changes in d-axis and q-axis currents caused by the transition process at the early stage of saturation, the time interval for the trajectory passing through the outer and middle blinders is $\Delta T = 0.0056s$, which is shorter than $\Delta T_{\text{PSB}} = 0.033s$. consequently, the PSB misidentifies the power swing event as a fault event, leading to a malfunction.

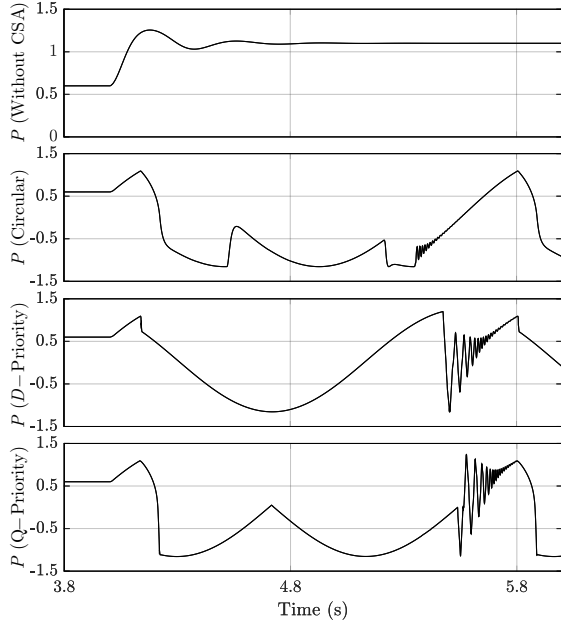


Fig. 11: Active power variations over time in Cases 1 to 4.

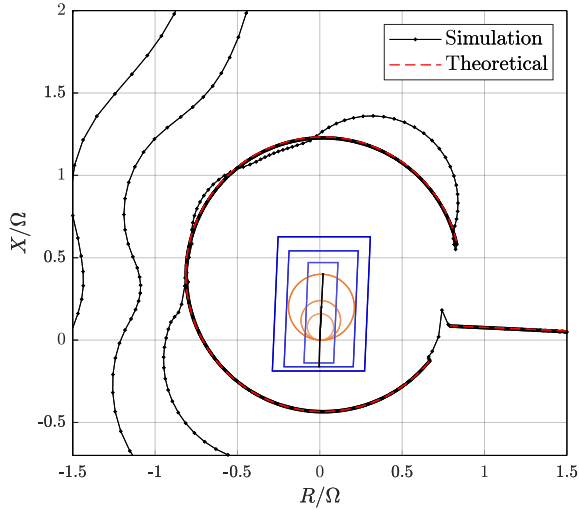


Fig. 12: The apparent impedance trajectory of Case 5.

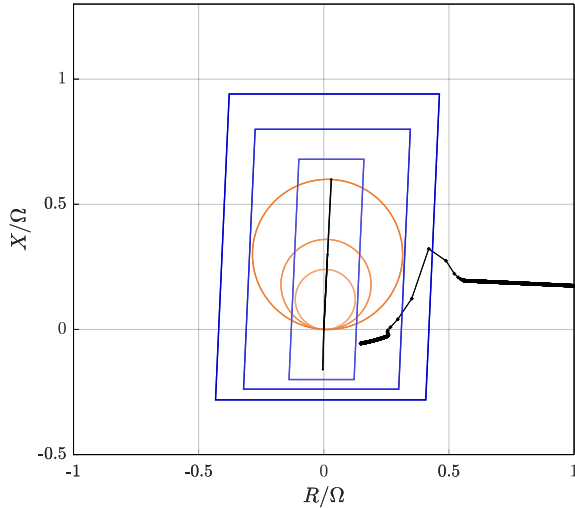


Fig. 13: The apparent impedance trajectory of Case 6.

D. The risk of being unable to exit saturation

In the d-axis priority CSA strategy shown in Fig. 9, there exists an SSEP. During the fault recovery process, the GFM IBR may become trapped at this SSEP, preventing successful recovery and leading to an undesirable outcome. This scenario is simulated in Case 7, with the conditions described as follows.

- Case 7: D-axis priority CSA. Phase jump of -216.76° at $t = 4s$.

The other conditions remain consistent with those in TABLE I. Fig. 14 illustrates the results of Case 7. The active power curve

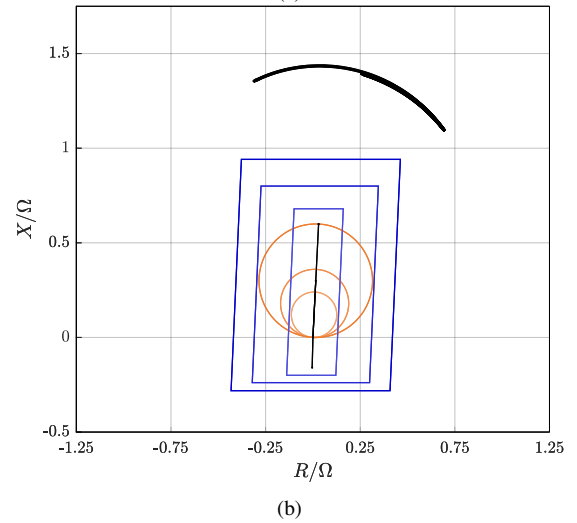
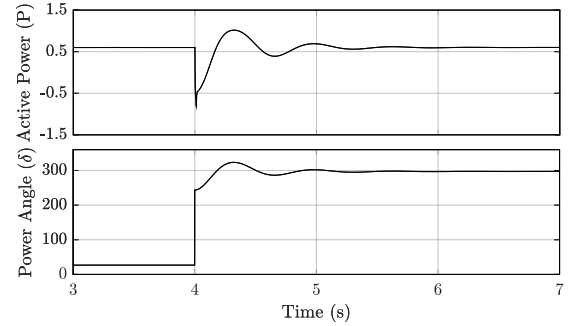


Fig. 14: The results of Case 7. (a) The curves of active power (p.u.) and power angle (unit: degrees) variations over time. (b) The apparent impedance trajectory.

in Fig. 14(a) shows that the GFM IBR can output the expected active power. However, the power angle fails to return to the original SEP but instead settles at a new SSEP. The apparent impedance trajectory, shown in Fig. 14(b) oscillates along the circular path before eventually stabilising at a point on the circle. This phenomenon is a unique feature introduced by the CSAs of the GFM IBR, which does not exist in conventional power swing detection schemes. Consequently, no existing scheme is currently capable of detecting and mitigating this situation.

VI. CONCLUSION

This paper provides a theoretical analysis of the conditions for current entering and exiting saturation under different

CSA-based current limiting strategies. Additionally, it investigates the differences in apparent impedance trajectories caused by CSAs compared to those in conventional SG-based systems. The conclusions are summarized as follows.

1) Circular and q-axis priority CSAs significantly reduce the stability margin, making it impossible for the system to return to the SEP after an event that causes the current to enter saturation. As a result, the system experiences an unstable power swing, severely deteriorating its stability.

2) The stability margin of the d-axis priority CSA is larger than that of circular and q-axis priority CSAs. However, under certain conditions, the circular power swing trajectory introduced by the CSA can cause both PSB and OST to fail. Additionally, the rapid current changes during the transient process after the current limiter is triggered may lead to a malfunction of PSB.

3) The d-axis priority CSA may cause the GFM IBR to become trapped in an SSEP. In this scenario, the current cannot exit saturation, leading the apparent impedance trajectory to stabilise at a point on the circular path. This is a unique feature introduced by the CSA-based current limiting strategy, which does not exist in conventional power swing detection schemes. Thus, this situation cannot be detected and mitigated.

REFERENCES

- [1] International Energy Agency, *World Energy Outlook 2024*. Paris: IEA, 2024, licence: CC BY 4.0 (report); CC BY NC SA 4.0 (Annex A). [Online]. Available: <https://www.iea.org/reports/world-energy-outlook-2024>
- [2] H. Zhang, W. Xiang, W. Lin, and J. Wen, "Grid forming converters in renewable energy sources dominated power grid: Control strategy, stability, application, and challenges," *Journal of Modern Power Systems and Clean Energy*, vol. 9, pp. 1239–1256, 11 2021.
- [3] R. H. Lasseter, Z. Chen, and D. Pattabiraman, "Grid-forming inverters: A critical asset for the power grid," *IEEE Journal of Emerging and Selected Topics in Power Electronics*, vol. 8, no. 2, pp. 925–935, 2020.
- [4] Y. Lin, J. H. Eto, B. B. Johnson, J. D. Flicker, R. H. Lasseter, H. N. Villegas Pico, G.-S. Seo, B. J. Pierre, and A. Ellis, "Research roadmap on grid-forming inverters," National Renewable Energy Lab.(NREL), Golden, CO (United States), Tech. Rep., 2020.
- [5] U. Muenz, S. Bhela, N. Xue, A. Banerjee, M. J. Reno, D. J. Kelly, E. Farantatos, A. Haddadi, D. Ramasubramanian, and A. Banaie, "Protection of 100% inverter-dominated power systems with grid-forming inverters and protection relays—gap analysis and expert interviews," Sandia National Lab.(SNL-NM), Albuquerque, NM (United States), Tech. Rep., 2024.
- [6] D. Hou, G. Benmouyal, and D. Tziouvaras, "Zero-setting power-swing blocking protection," in *3rd IEE international conference on reliability of transmission and distribution networks (RTDN 2005)*. IET, 2005, pp. 249–254.
- [7] IEEE Power System Relaying and Control Committee (PSRC) Working Group WG-D6, "Power swing and out-of-step considerations on transmission lines," PSRC, Tech. Rep., Jul. 2005, [Online]. Available: <https://bit.ly/3kQx8xI>
- [8] System Protection and Control Subcommittee, "Protection system response to power swings," NERC, Atlanta, USA, Tech. Rep., Aug. 2013, [Online]. Available: <https://www.bit.ly/3IG62Jv>
- [9] A. Haddadi, I. Kocar, E. Farantatos, and J. Mahseredjian, "EPRI technical report: System protection guidelines for systems with high levels of renewables: Impact of wind & solar generation on negative-sequence and power swing protection," EPRI, Tech. Rep., 12 2017.
- [10] N. Fischer, G. Benmouyal, D. Hou, D. Tziouvaras, J. Byrne-Finley, and B. Smyth, "Tutorial on power swing blocking and out-of-step tripping," in *Proceedings of the 39th Annual Western Protective Relay Conference*, 2012, pp. 1–20.
- [11] GE, *D60 Line Distance Protection System: Instruction Manual*, Markham, Canada, Jun. 2023, [Online]. Available: <https://bit.ly/3mucHXR>
- [12] Hitachi Energy, *Line Distance Protection REL670, Version 2.2 ANSI: Application Manual*, 2024, [Online]. Available: <https://bit.ly/3abcXYZ>
- [13] Siemens, *SIPROTEC 5, Distance Protection, 7SA82-V9.5: Manual*, Germany, Apr. 2023, [Online]. Available: <https://sie.ag/44MKLPU>
- [14] I. S. Association, "IEEE guide for protective relay applications to transmission lines," *IEEE Std C37.113-2015 (Revision of IEEE Std C37.113-1999)*, pp. 1–141, 2016.
- [15] B. Fan, T. Liu, F. Zhao, H. Wu, and X. Wang, "A review of current-limiting control of grid-forming inverters under symmetrical disturbances," *IEEE Open Journal of Power Electronics*, vol. 3, pp. 955–969, 2022.
- [16] T. Qoria, F. Gruson, F. Colas, X. Kestelyn, and X. Guillaud, "Current limiting algorithms and transient stability analysis of grid-forming vscs," *Electric Power Systems Research*, vol. 189, p. 106726, 2020. [Online]. Available: <https://www.sciencedirect.com/science/article/pii/S0378779620305290>
- [17] E. Rokrok, T. Qoria, A. Bruyere, B. Francois, and X. Guillaud, "Transient stability assessment and enhancement of grid-forming converters embedding current reference saturation as current limiting strategy," *IEEE Transactions on Power Systems*, vol. 37, no. 2, pp. 1519–1531, 2022.
- [18] B. Fan and X. Wang, "Fault recovery analysis of grid-forming inverters with priority-based current limiters," *IEEE Transactions on Power Systems*, vol. 38, no. 6, pp. 5102–5112, 2023.
- [19] Y. Li, Y. Lu, J. Yang, X. Yuan, R. Yang, S. Yang, H. Ye, and Z. Du, "Transient stability of power synchronization loop based grid forming converter," *IEEE Transactions on Energy Conversion*, vol. 38, no. 4, pp. 2843–2859, 2023.
- [20] Y. Lu, Y. Li, T. Mu, C. Shao, J. Liu, D. Yang, and Z. Du, "Segmental equal area criterion for grid forming converter with current saturation," *International Journal of Electrical Power & Energy Systems*, vol. 159, p. 110015, 2024. [Online]. Available: <https://www.sciencedirect.com/science/article/pii/S0142061524002369>
- [21] A. Arjomandi-Nezhad, Y. Guo, B. C. Pal, and G. Yang, "Modeling fault recovery and transient stability of grid-forming converters equipped with current reference limitation," *IEEE Transactions on Energy Conversion*, pp. 1–13, 2024.
- [22] A. Haddadi, I. Kocar, U. Karaagac, H. Gras, and E. Farantatos, "Impact of wind generation on power swing protection," *IEEE Transactions on Power Delivery*, vol. 34, no. 3, pp. 1118–1128, 2019.
- [23] A. Haddadi, E. Farantatos, I. Kocar, and U. Karaagac, "Impact of inverter based resources on system protection," *Energies*, vol. 14, p. 1050, 02 2021.
- [24] J. T. Rao, B. R. Bhalja, M. V. Andreev, and O. P. Malik, "Synchrophasor assisted power swing detection scheme for wind integrated transmission network," *IEEE Transactions on Power Delivery*, vol. 37, no. 3, pp. 1952–1962, 2022.
- [25] M. Jayamohan, S. Das, and S. Brahma, "Impedance trajectories during stable and unstable power swings in presence of pq control based pv generations," in *2023 IEEE Power & Energy Society General Meeting (PESGM)*. IEEE, 2023, pp. 1–5.
- [26] M.-A. Nasr and A. Hooshyar, "Power swing in systems with inverter-based resources—part i: Dynamic model development," *IEEE Transactions on Power Delivery*, vol. 39, no. 3, pp. 1889–1902, 2024.
- [27] M.-A. Nasr and A. Hooshyar, "Power swing in systems with inverter-based resources—part ii: Impact on protection systems," *IEEE Transactions on Power Delivery*, vol. 39, no. 3, pp. 1903–1917, 2024.
- [28] Y. Xiong, H. Wu, Y. Li, and X. Wang, "Comparison of power swing characteristics and efficacy analysis of impedance-based detections in synchronous generators and grid-following systems," *IEEE Transactions on Power Systems*, pp. 1–12, 2024.
- [29] Y. Xiong, H. Wu, and X. Wang, "Efficacy analysis of power swing blocking and out-of-step tripping protection for grid-following-vsc systems," in *2023 8th IEEE Workshop on the Electronic Grid (eGRID)*. IEEE, 2023, pp. 1–5.
- [30] Y. Xiong, H. Wu, and X. Wang, "Efficacy analysis of legacy dual-blinder-based power swing detection scheme in grid-forming vsc-based power system," *IET Conference Proceedings*, vol. 2023, pp. 763–768, 2023. [Online]. Available: <https://digital-library.theiet.org/doi/abs/10.1049/icp.2023.2815>
- [31] P. Kundur, *Power System Stability and Control*. New York, NY, USA: McGraw-Hill, 1994.